The Astrophysical Journal, 800:108 (6pp), 2015 February 20 doi:10.1088/0004-637X/800/2/108

DUST ATTENUATION IN HIGH REDSHIFT GALAXIES: "DIAMONDS IN THE SKY"

Nick Scoville[1], Andreas Faisst[2], Peter Capak[1,3], Yuko Kakazu[4], Gongjie Li[5], and Charles Steinhardt[1,3]
[1] California Institute of Technology, MC 249-17, 1200 East California Boulevard, Pasadena, CA 91125, USA
[2] Institute for Astronomy, Swiss Federal Institute of Technology (ETH Zurich), CH-8093 Zurich, Switzerland
[3] Infrared Processing and Analysis Center (IPAC), 1200 East California Boulevard, Pasadena, CA 91125, USA
[4] Subaru Telescope, 650 North A'ohoku Place, Hilo, HI 96720, USA
[5] Harvard-Smithsonian Center for Astrophysics, The Institute for Theory and Computation, 60 Garden Street, Cambridge, MA 02138, USA
Received 2014 October 27; accepted 2014 December 27; published 2015 February 18

ABSTRACT

We use observed optical to near-infrared spectral energy distributions (SEDs) of 266 galaxies in the COSMOS survey to derive the wavelength dependence of the dust attenuation at high redshift. All of the galaxies have spectroscopic redshifts in the range $z = 2$–6.5. The presence of the C IV absorption feature, indicating that the rest-frame UV–optical SED is dominated by OB stars, is used to select objects for which the intrinsic, unattenuated spectrum has a well-established shape. Comparison of this intrinsic spectrum with the observed broadband photometric SED then permits derivation of the wavelength dependence of the dust attenuation. The derived dust attenuation curve is similar in overall shape to the Calzetti curve for local starburst galaxies. We also see the 2175 Å bump feature which is present in the Milky Way and Large Magellanic Cloud extinction curves but not seen in the Calzetti curve. The bump feature is commonly attributed to graphite or polycyclic aromatic hydrocarbons. No significant dependence is seen with redshift between sub-samples at $z = 2$–4 and $z = 4$–6.5. The "extinction" curve obtained here provides a firm basis for color and extinction corrections of high redshift galaxy photometry.

Key words: cosmology: observations – dust, extinction – Galaxy: evolution – galaxies: high-redshift – ISM: clouds

1. INTRODUCTION

Dust profoundly affects the light emitted from galaxies—requiring large corrections for extinction in the UV and optical. This causes a severe degeneracy in the derived ages of high redshift galaxies and hence results in a major uncertainty in their derived properties. The extinction has a major effect on the observability of the galaxies and on their derived stellar masses, star formation rates, and luminosities. At early epochs there is an increasing fraction of active star-forming galaxies compared to the low redshift local galaxy population. The observed properties of these star-forming galaxies are strongly dependent on the dust extinction since many of the surveys probe the rest-frame UV, where the dust extinction is higher than at visible wavelengths. The amount of dust extinction is almost always inferred from the differential extinction or reddening. Translating this reddening into an estimate of the total extinction at any wavelength then requires knowledge of the dust extinction curve as a function of wavelength.

At low redshifts the extinction curve has been determined along many lines-of-sight in the Galaxy (cf. Savage & Mathis 1979) and at lower metallicities it has been determined along the Large Magellanic Cloud (LMC) and Small Magellanic Cloud (SMC; Prevot et al. 1984; Fitzpatrick 1986). The mean extinction curves for each of these galaxies are quite different: the SMC curve has the steepest power-law form and no 2175 Å bump, whereas both the LMC and the Milky Way extinction curves show the 2175 Å feature and the Milky Way has the flattest overall wavelength dependence (Gallerani et al. 2010). The SMC has the lowest metallicity of the three galaxies and this probably results in a different grain composition and/or size distribution. These large differences underscore the critical importance of empirical determination of the reddening curves at high redshifts. An effective extinction curve for the integrated light from galaxies was obtained by Calzetti et al. (1994, 1996) and this is commonly used for analysis of high redshift galaxies.

Direct determination of the differential extinction curve in high-z galaxies has been difficult using just photometry since one needs to break the age/reddening degeneracy in the observed galaxies and this cannot be done without prior assumption of a form for the extinction curve. Kriek & Conroy (2013) fit a grid of spectral energy distribution (SED) templates and power-law attenuation curves to the photometry of a sample of galaxies at $z = 0.5$ to 2. They used the broad- and intermediate-band photometry to classify the intrinsic SED type of each galaxy and then correlated the extinction curve slope and the 2175 Å bump strength with galaxy type. A similar procedure, fitting a library of SED templates, was employed by Buat (2013) to analyze a sample of galaxies at $z = 0.95$–2.2. Their favored attenuation curve was similar to that in the LMC super-shell region.

The approach we advocate here relies upon the intrinsic or un-extincted spectrum of the stellar population being known or identified a priori from high resolution spectroscopic features. Then, the differential extinction can be easily derived by comparison of the observed SEDs (obtained from broadband photometry) with that of the intrinsic spectrum. In fact, there is a UV spectral signature that clearly identifies the nature of the intrinsic spectrum: the C IV absorption feature at $\lambda = 1549$ Å. The C IV absorption indicates the presence of type O and supergiant B stars and when the C IV absorption is strong, such stars dominate the UV continuum emission.

The C IV absorption feature in the spectra of high redshift galaxies in the COSMOS survey thus selects objects for which the broadband photometry can be used to determine the differential extinction curve. For such galaxies, the C IV absorption implies that the UV–optical SED is dominated by OB stars and the overall slope of the intrinsic (un-extincted) continuum SED is known.

We use a sample of 266 galaxies at $z = 2$–6.5 for which rest-frame UV spectroscopy shows the C IV absorption to analyze the wavelength dependence of the dust attenuation. Starburst

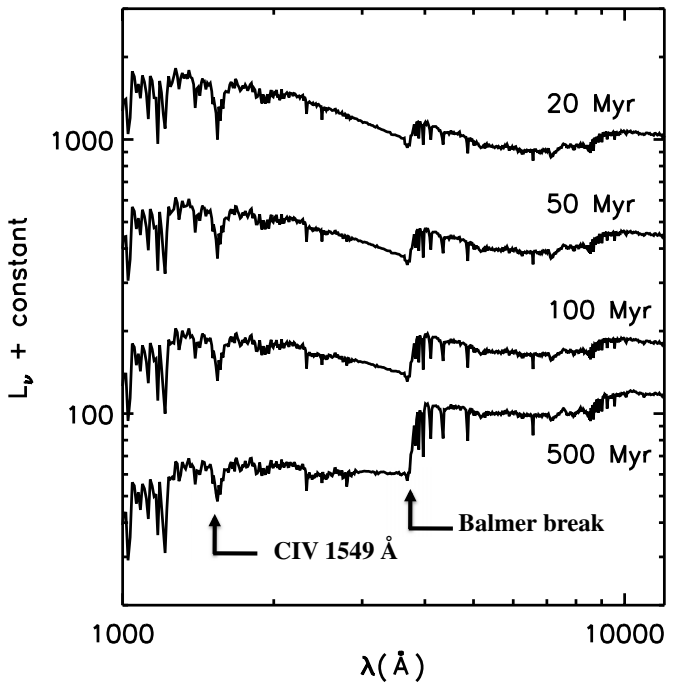

Figure 1. Simulated spectra for *constant* star formation rate (SFR) starbursts of duration 20–500 Myr obtained using Starburst99 with a Kroupa IMF and solar metallicity. The strong C IV absorption at $\lambda = 1549$ Å seen in these spectra requires significant SF within the previous 10 Myr since this feature is produced in O-type stars. The overall shape of the SED is relatively invariant for the first ∼50 Myr; after that time, the Balmer break at $\lambda = 3646$ Å becomes more pronounced and thus causes the broadband SED to change in shape. Any objects with a Balmer break larger than 25%, corresponding to spectra with ages exceeding that of the model shown with 100 Myr age, were removed from our sample. Here we use the combination of a strong C IV absorption plus the absence of a strong Balmer/4000 Å break to select sources to illuminate the dust attenuation.

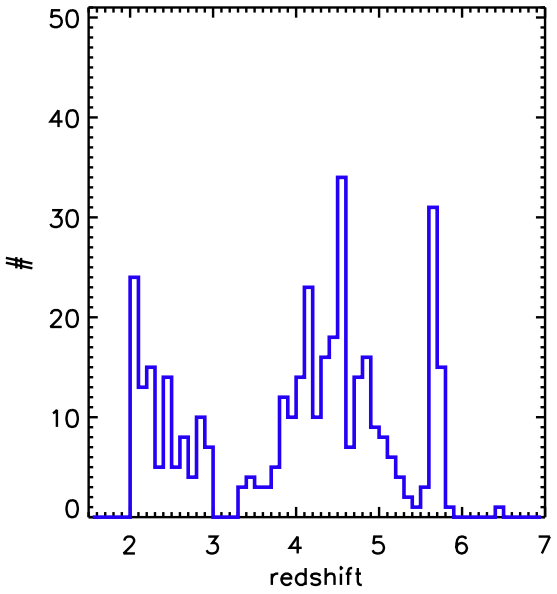

Figure 2. Spectroscopic redshift distribution of galaxies in our sample.

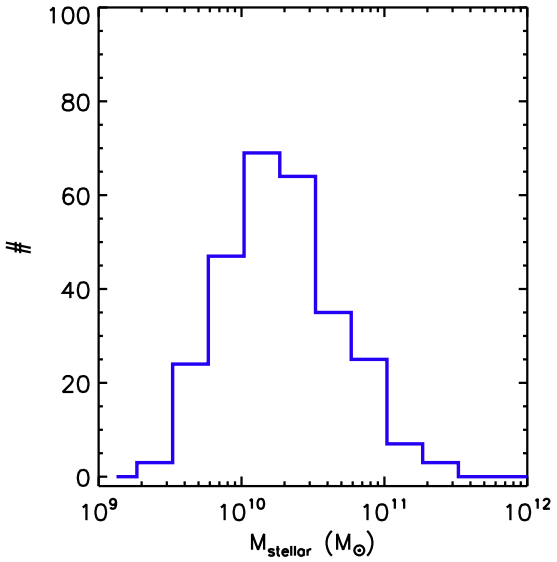

Figure 3. Stellar mass distribution of galaxies in our sample. The masses were derived from SED template fitting to the photometry using the ZEBRA+ code with a constant SFH, a Chabrier IMF (similar to Kroupa), and a metallicity range from $Z = 0.005, 0.001, 0.01$.

(SB) model simulations in Section 2 define the age range (up to ∼50 Myr) of stellar populations for which the C IV absorption can be used as a signpost for the overall SED. In Section 3 we describe the galaxy sample used for this study and then outline the numerical technique in Section 4. The derived attenuation curve is presented in Section 5 and discussed in Section 6.

2. C IV ABSORPTION AS A SIGNPOST FOR THE SED

In Figure 1 spectra of SB stellar populations are shown for *constant* star formation rates extending from 20 to 500 Myr. These spectra were generated using the Starburst99 simulation tool (Leitherer et al. 1999) with solar metallicity and a Kroupa initial mass function (IMF) for the stars. The strongest spectral feature in these plots is the C IV absorption at $\lambda = 1549$ Å; this absorption is produced in the atmospheres and outflow winds of O stars and is present as long as O-type stars dominate the rest-frame UV emission. In an instantaneous SB, the feature will diminish rapidly since the typical lifetime of those stars is $\leqslant$10 Myr. Hence, this feature is a robust signpost of ongoing OB star formation. Then, the UV–optical continuum, dominated by OB stars, has a quite constant SED shape.

At longer wavelengths, the dominant spectral feature is the Balmer break at $\lambda = 3646$ Å. As the stellar population ages, or as the fraction of intermediate mass stars grows, this feature becomes more pronounced, causing the optical SED shape to evolve, specifically becoming redder at later epochs.

At early epochs ($\lesssim$20–100 Myr) the spectra are very constant in both broadband shape and spectral features (see Figure 1) and such sources may be used as background sources to probe the wavelength dependence of the foreground dust attenuation. The signatures of appropriate galaxies to select are: (1) the detection of C IV absorption and (2) the absence of a strong Balmer/4000 Å break feature. The C IV absorption feature at $\lambda = 1549$ Å is also seen in type 2 active galactic nucleus (AGN) sources, but these can be recognized using AGN signatures such as X-ray and strong radio emission or nuclear point sources. These discriminants against AGNs may not catch all AGNs at the highest redshifts given the limited sensitivity of X-ray and radio data. The C IV absorption is very strong and hence easily detected. For a Kroupa IMF, the C IV equivalent width is ∼9.5 Å at early times; it can therefore be easily seen down to 1/10 solar

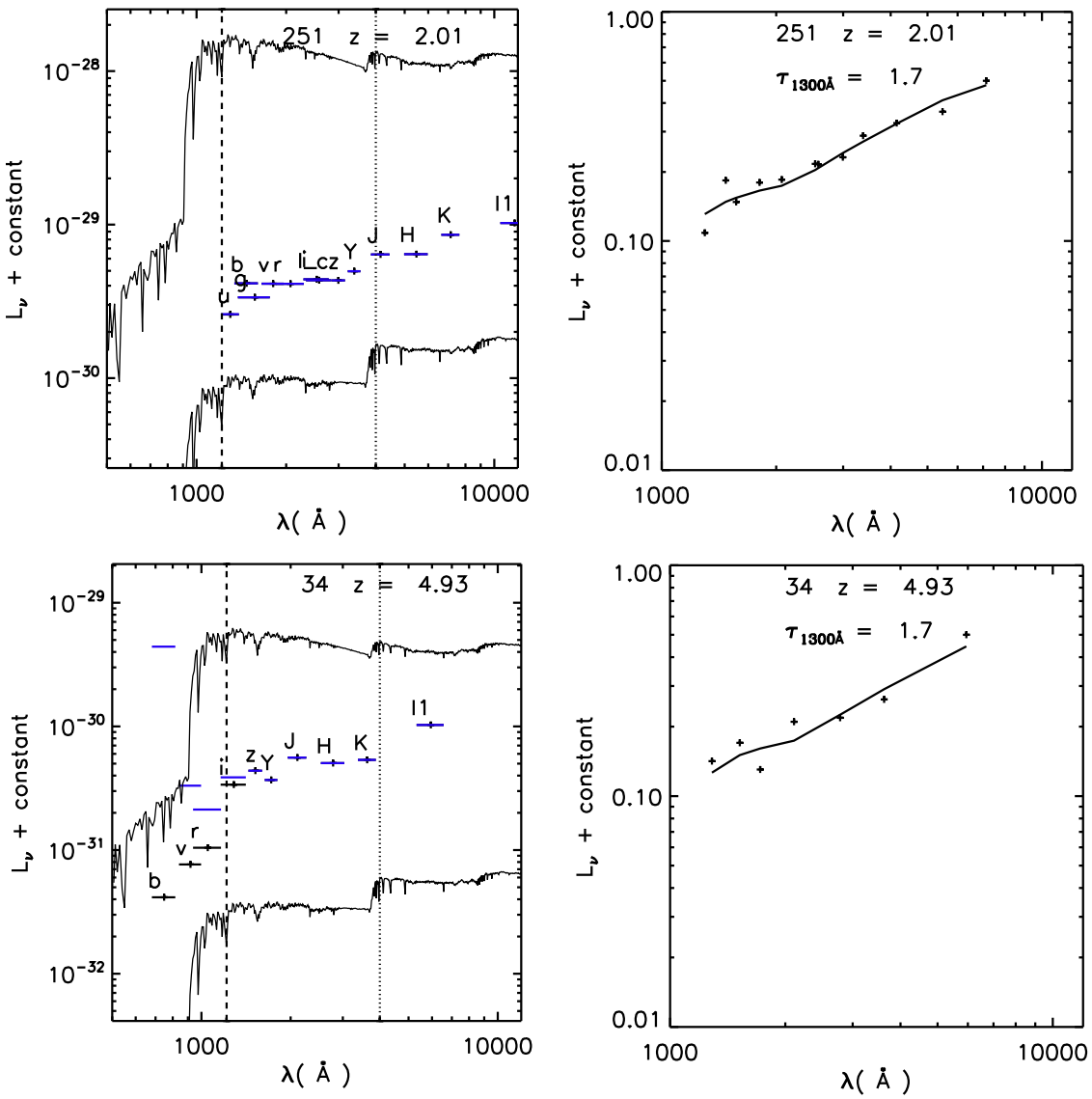

Figure 4. Left: the rest-frame SEDs are shown for two sources at $z = 2.01$ and 4.93. The constant rate SB spectra are shown for ages of 50 and 500 Myr for comparison. The dashed and dotted lines correspond to 1216 Å and 4000 Å. Right: the best-fit SEDs using the derived wavelength dependence of the attenuation (normalized to the reference wavelength $\lambda = 1300$ Å) and an absolute value of the optical depth $\tau_{1300\,\text{Å}} = 1.7$ (coincidentally in both instances). Although the best-fit curve extends to 950 Å, these plots limit the spectral range of the curve to wavelengths for which each source has photometry.

metallicity. This was confirmed by additional SB simulations not shown here.

3. GALAXY SAMPLE SELECTION

Our source sample is drawn from the COSMOS survey field, with the primary selection being those objects with spectroscopic coverage from our Keck DEIMOS survey (PI: N. Scoville). This survey includes ~2300 galaxies at $z = 2$–6.5 down to $I_{AB} = 25$ mag. From this sample, we then selected only those objects with the C IV absorption feature and at least six broadband continuum photometric detections (average is 10.3 photometric bands for each source). The redshifts were determined from the C IV absorption plus other emission lines and we required at least two lines for a reliable spectroscopic redshift. As noted in Section 2, we then removed from further consideration any objects exhibiting a Balmer break larger than 25% in flux. The final fitting included 266 objects at $z = 2$–6.5 and then subsamples of 135 and 132 objects at $z = 2$–4 and 4–6.5.[6] The redshift and stellar mass distributions of sources are shown in Figures 2 and 3.

The COSMOS photometry used here includes the 34 band photometry used for the COSMOS photometric redshifts (Ilbert et al. 2013) and the near-infrared deep photometry from UltraVista (McCracken et al. 2012) and *Spitzer* SPLASH (Steinhardt et al. 2014). For the attenuation curve analysis here, we use the 14 broad bands ($u_{\rm CFHT}$, $B_{\rm Subaru}$, $V_{\rm Subaru}$, $g_{\rm Subaru}$, $r_{\rm Subaru}$, $i_{\rm Subaru}$, $z_{\rm Subaru}$, $I_{\rm CFHT}$, IRAC1, IRAC2, $Y_{\rm Ultra-Vista}$, $J_{\rm Ultra-Vista}$, $H_{\rm Ultra-Vista}$, $K_{\rm Ultra-Vista}$) with the highest signal-to-noise ratios (see Table 1; Ilbert et al. 2009). At least six bands were required in the rest wavelength range between Lyman α (1216 Å) and 10000 Å. In addition, we required at least one detection on each side of the Balmer/4000 Å break.

[6] The source list is available in an ASCII table from the COSMOS data archive at IPAC/IRSA: http://irsa.ipac.caltech.edu/data/COSMOS/tables/extinction/extinction_curve_source_list.dat.

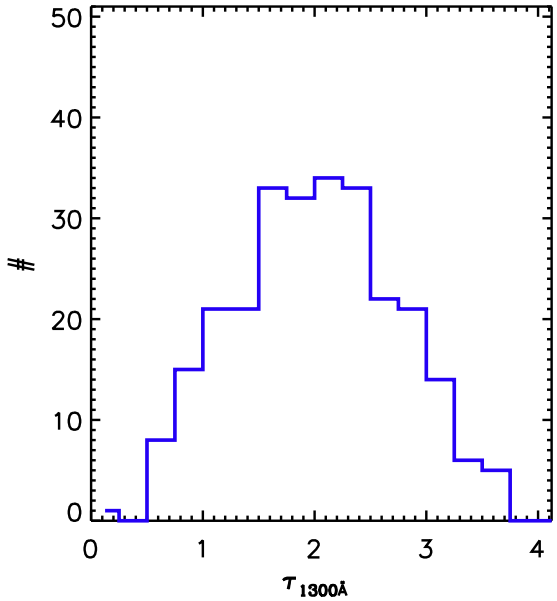

Figure 5. Distribution of derived $\tau_{1300\,\text{Å}}$ is shown for the full sample at $z = 2$–6.5.

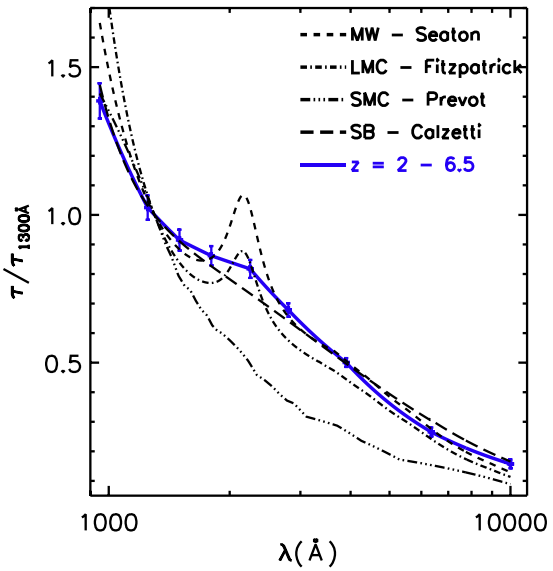

Figure 6. Wavelength dependence of the attenuation is shown for the full sample spanning $z = 2$–6.5 with uncertainties determined from the Levenberg–Marquardt routine. Also shown are the extinction curves for the Milky Way (Seaton 1979), LMC (Fitzpatrick 1986), SMC (Prevot et al. 1984), and local SB galaxies (Calzetti et al. 2000). The wavelength dependence derived here for galaxies at $z > 2$ is similar to that of the Calzetti curve derived for SB galaxies but also includes the 2175 Å bump feature as seen in the Milky Way and LMC extinction curves.

For rest wavelengths short of Lyman α there is significant intergalactic medium (IGM) H I absorption at the higher redshifts. At these wavelengths we corrected the photometry to brighter values using the standard Madau correction (Madau 1995). This correction has a very large dispersion (see Madau 1995) and we found that it clearly overcorrected the photometry as indicated from the fact that the corrected fluxes short of Lyα exceeded those of adjacent bands just longward of Lyα. Reducing the Madau correction by 50% avoids this. The derived dust attenuation at the one point short of 1216 Å should therefore be viewed with some uncertainty since it hinges on the values of the IGM H I correction.

Sample SEDs for two such objects at $z = 2.01$ and 4.93 are shown on the left in Figure 4 together with the constant rate SB spectra for 50 and 500 Myr duration for reference.

4. NUMERICAL SOLUTION

We assume that the dust attenuation has a wavelength dependence common to all sources in each redshift sample, but that the absolute value of the dust optical depth at a fiducial wavelength is freely varying between sources. Thus, the wavelength dependence is characterized by a step function ($\tau(\lambda_i)$) with discrete wavelength bins spanning rest-frame $\lambda = 950$ and 10000 Å. This form of fitting has the virtue of making no assumption or analytic parameterization of the extinction. In addition, there is an absolute source-dependent scale factor for the optical depth at rest-frame $\lambda = 1300$ Å($\tau_{1300\,\text{Å}}$). Thus,

$$\tau_\lambda(\text{source}) = \tau_{1300\,\text{Å}}(\text{source})\tau(\lambda_i). \quad (1)$$

For the normalized opacity function ($\tau(\lambda_i)$), we use nine bins spaced logarithmically in wavelength. If the rest-frame specific luminosity of the unobscured SB is denoted as l_ν(SB), then the model we fit to the observed SEDs is given by

$$s_\nu = e^{-\tau_\lambda(\text{source})} L_0(\text{source}) l_\nu(\text{SB}). \quad (2)$$

The underlying source SED (l_ν(SB)) is taken to be the 50 Myr SB spectrum shown in Figure 1 based on our deselection of sources with a larger Balmer break, as measured from the best-fit stellar population model to the photometry. We did experiment using the 20 and 100 Myr SEDs and they did not improve the resultant best-fit χ^2.

For the $z = 2$–6.5 sample of 266 galaxies, the number of free parameters to be solved for in minimized χ^2 is: 266 (L_0(source)) + 266 ($\tau_{1300\,\text{Å}}$(source)) + 9 (wavelength bins) = 541 parameters. For this minimization, we used the Levenberg–Marquardt least-squares minimization routine

Table 1
Best-fit Attenuation Curve

λ (Å)	$z = 2$–6.5 τ_λ/τ_{1300}	$z = 2$–4 τ_λ/τ_{1300}	$z = 4$–6.5 τ_λ/τ_{1300}
950	1.386 ± 0.060	1.406 ± 0.053	1.431 ± 0.026
1250	1.025 ± 0.041	1.028 ± 0.035	0.999 ± 0.024
1500	0.915 ± 0.035	0.904 ± 0.029	1.003 ± 0.025
1800	0.862 ± 0.033	0.850 ± 0.026	0.924 ± 0.030
2250	0.817 ± 0.030	0.826 ± 0.025	0.865 ± 0.043
2800	0.678 ± 0.023	0.706 ± 0.019	0.716 ± 0.061
3900	0.501 ± 0.015	0.530 ± 0.012	0.509 ± 0.073
6350	0.266 ± 0.016	0.363 ± 0.011	0.255 ± 0.092
10000	0.158 ± 0.017	0.181 ± 0.014	0.127 ± 0.096
No. of galaxies[a]	266	135	132
No. of phot. bands[b]	2747	1614	1133
χ^2	3.68	1.92	6.63

Notes. As described in the text, the least-squares fitting solved for the wavelength dependence as a step function so that each wavelength point is independent, and smoothness of continuity is not enforced except if warranted by the data. The attenuation curves were each normalized to unity at $\lambda = 1330$ Å.

[a] Number of galaxies in the final samples for the fit. The samples were slightly larger on the first pass fitting; after the first pass, 5–15 galaxies with $\tau_{1300\,\text{Å}} > 5$ were removed for the second pass fitting since their short wavelength points would have low signal-to-noise ratios. Removing these sources reduced the χ^2 but did not significantly change the shape of the attenuation curve.

[b] Total number of photometric band fluxes used in fitting.

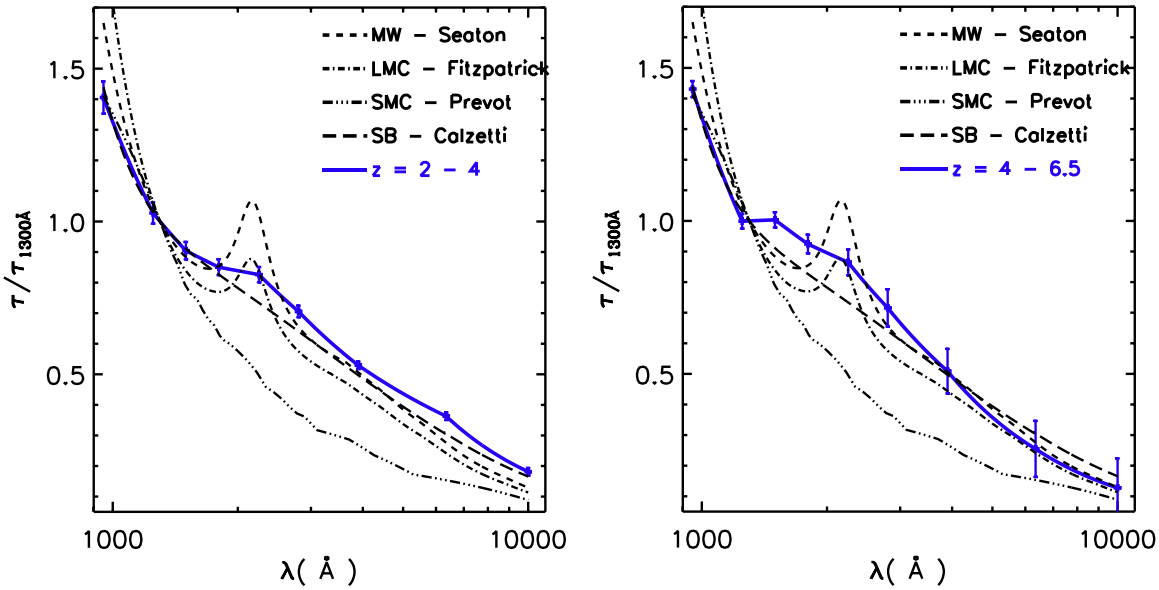

Figure 7. Wavelength dependence of the attenuation is shown for sub-samples at $z = 2$–4 (left) and 4–6.5 (right). Given the larger uncertainties in the $z = 4$–6.5 fit, we do not think the difference in the 2175 Å bump feature is significant. The overall broadband wavelength dependencies are more consistent with the MW, LMC, and SB curves and not with the SMC curve.

(MPFIT in IDL). We adopted uncertainties of 10% for each SED data point; this was done to give all SED points similar weight in the fitting. Thus, we avoid overweighting a single band that has a high signal-to-noise ratio but does not provide much wavelength leverage. This ensures that the IRAC data (3.6 μm and 5.8 μm) constrain the fit at long wavelengths.

The least-squares fitting was done in two passes: first using the complete sample of galaxies and then removing the few objects ($\sim$10) that had $\tau_{1300} > 5$; these latter sources are likely to have low signal-to-noise ratios at the short wavelengths. The derived results were not significantly different after the second pass except that the χ^2 was improved slightly ($\leqslant$10%). Figure 5 shows the distribution of derived $\tau_{1300\,\text{Å}}$ of the final solution.

5. RESULTS

The derived spectral dependence of the normalized dust attenuation is shown in Figure 6 for the full sample at $z = 2$–6.5. The uncertainties on the attenuation curve shown in the figure are from the Levenberg–Marquardt algorithm. The χ^2 for the fits in the three redshift ranges are given in Table 1 are 3.7, 1.9, and 6.6. For the fitting, the uncertainties on each flux measurement were set to 10%, thus the derived fits typically disperse only 13%–25% from the observed fluxes on all of the individual sources.

Also shown are the extinction curves for the Milky Way, LMC, and SMC plus the dust attenuation curve for SB galaxies from Calzetti et al. (2000). All curves were normalized to their values at 1300 Å. The overall wavelength dependence of the attenuation curve for $z = 2$–6.5 is remarkably similar to that of the low redshift attenuation curve for the SB galaxies. It is also very similar to the extinction curves for the Milky Way and LMC, but not the SMC, which has a much stronger wavelength dependence in the UV. Table 1 lists the numeric values for the derived attenuation curves.

The high redshift curve (Figure 6, Table 1) also clearly shows the presence of the 2175 Å bump feature seen in the Milky Way and the LMC extinction curves but not in the SBs or the SMC. This feature is often attributed to graphite (hence the word "diamonds" in the title of this paper) grains and its absence in the SMC extinction curve is probably related to the low metallicity of the SMC, resulting in different grain properties. The absence of the 2175 Å bump feature in the Calzetti curve (derived for local SB galaxies) is certainly significant in Calzetti et al. (1994) (see Figure 17 there).

In order to probe the redshift evolution of the attenuation, we also obtained solutions for sub-samples of the galaxies at $z = 2$–4 and $z = 4$–6.5. The results are shown in Figure 7. Their attenuation curves do not appear significantly different from that shown in Figure 6 for the full sample. The $z = 4$–6.5 curve exhibits a somewhat larger width for the 2175 Å bump feature but we do not consider this significant given the uncertainties.

6. SUMMARY AND COMMENTS

Our technique uses galaxies selected spectroscopically with strong CIV absorption and photometrically with a small Balmer/4000 Å break feature to yield a sample of galaxies for which the un-extincted UV–optical SEDs are dominated by OB stars. These SEDs have a nearly constant shape since their emission over the entire wavelength is from a single class of stars. Our sample of galaxies taken from the large COSMOS survey field; it consists of 266 sources after removing sources with incomplete wavelength coverage.

The derived attenuation is very similar to the Calzetti et al. (2000) curve obtained for 40 low redshift SB galaxies. The curve shown in Figure 6 clearly shows the 2175 Å bump feature; this was not present in the Calzetti curve, but is seen in both the Milky Way and the LMC. Our curve is tabulated in Table 1 for use in correcting colors and extinctions from high redshift galaxy surveys, both star-forming and non-star-forming galaxies.

It is important to remember that the curves shown here for the MW, LMC, and SMC were all obtained from line-of-sight extinction measurements of stars. In contrast, the SB curve (Calzetti et al. 2000) and that derived here for high redshift are "effective attenuation" curves—they are obtained from the integrated galaxy light. The former extinction curves include the effects of both dust absorption and scattering while the effective

attenuation curves may contain a lesser contribution from dust scattering (since some photons are scattered back into our line-of-sight). The attenuation curves also include the very important effect of partial covering of the galactic continuum by dust in the line-of-sight. This is, of course, not relevant to extinction measurements of individual stars.

Two other instances where the high redshift attenuation/extinction curve has been analyzed are for gamma-ray burst (GRB) sources and QSOs. Elíasdóttir et al. (2009) obtained an extinction curve for GRB 070802 at $z = 2.45$ which was similar to the LMC extinction curve shown in Figure 4, including the 2175 Å bump at high signal-to-noise ratios. Perley et al. (2011) also clearly detected the 2175 Å feature in GRB 080607 at $z = 3.03$.

In contrast to the GRBs and the SB galaxies analyzed here, the high redshift QSOs show quite different extinction curves. They generally resemble the SMC extinction curve (Richards et al. 2003; Reichard et al. 2003; Hopkins et al. 2004), not the LMC, Milky Way, or SB curves. This said, Gallerani et al. (2010) analyzed the dust extinction in a sample of 39 quasars at $z = 3.9$–6.4 and found a substantially flatter extinction curve at $\lambda < 1300$ Å than the SMC curve. In fact, their extinction curve is flatter than the Calzetti curve at $\lambda < 2500$ Å, implying that it is also flatter than that obtained here at high redshift. They see no evidence of the 2175 Å bump feature, although in many of their quasars this feature might be difficult to detect due to the broad QSO emission lines. In the quasars, the obscuration occurs from three distinct regions: the inner region with gas only seen in the X-rays, the mid-IR very hot dust within a few parsecs of the AGN, and the host galaxy dust (Elvis 2012). In the first two regions, the dust abundance and composition is likely to be very different.

An alternative, future application of the technique developed here would be possible if high quality spectra became available over the UV–optical wavelength range on a small number of bright sources. Then, accurate measures of the equivalent width of the C IV spectral feature and the Balmer break strength could be used to select more precisely the source SED templates for each individual source.

We thank the referee for suggestions and Martin Elvis for comments on an early draft. We also thank Zara Scoville for proofreading the manuscript. A.F. acknowledges support from the Swiss National Science Foundation and thanks Caltech for hospitality while working on this article.

REFERENCES

Buat, V. 2013, EP&S, 65, 1095
Calzetti, D., Armus, L., Bohlin, R. C., et al. 2000, ApJ, 533, 682
Calzetti, D., Kinney, A. L., & Storchi-Bergmann, T. 1994, ApJ, 429, 582
Calzetti, D., Kinney, A. L., & Storchi-Bergmann, T. 1996, ApJ, 458, 132
Elíasdóttir, Á., Fynbo, J. P. U., Hjorth, J., et al. 2009, ApJ, 697, 1725
Elvis, M. 2012, JPhCS, 372, 012032
Fitzpatrick, E. L. 1986, AJ, 92, 1068
Gallerani, S., Maiolino, R., Juarez, Y., et al. 2010, A&A, 523, A85
Hopkins, P. F., Strauss, M. A., Hall, P. B., et al. 2004, AJ, 128, 1112
Ilbert, O., Capak, P., Salvato, M., et al. 2009, ApJ, 690, 1236
Ilbert, O., McCracken, H. J., Le Fèvre, O., et al. 2013, A&A, 556, A55
Kriek, M., & Conroy, C. 2013, ApJL, 775, L16
Leitherer, C., Schaerer, D., Goldader, J. D., et al. 1999, ApJS, 123, 3
Madau, P. 1995, ApJ, 441, 18
McCracken, H. J., Milvang-Jensen, B., Dunlop, J., et al. 2012, A&A, 544, A156
Perley, D. A., Morgan, A. N., Updike, A., et al. 2011, AJ, 141, 36
Prevot, M. L., Lequeux, J., Prevot, L., Maurice, E., & Rocca-Volmerange, B. 1984, A&A, 132, 389
Reichard, T. A., Richards, G. T., Hall, P. B., et al. 2003, AJ, 126, 2594
Richards, G. T., Hall, P. B., Vanden Berk, D. E., et al. 2003, AJ, 126, 1131
Savage, B. D., & Mathis, J. S. 1979, ARA&A, 17, 73
Seaton, M. J. 1979, MNRAS, 187, 73P
Steinhardt, C. L., Speagle, J. S., Capak, P., et al. 2014, ApJL, 791, L25